

Sunflower-Like SrCo_2S_4 @f-MWCNTs Hybrid Wrapped by Engineering N-Reduced Graphene Oxide for High Performance Dye-Sensitized Solar Cells

Weiming Zhang¹, Muhammad Wasim Khan¹, Xueqin Zuo¹, Qun Yang¹, Huaibao Tang^{1,2},
Shaowei Jin^{1,2} and Guang Li^{1,2,3,*}

¹School of Physics and Materials Science, Anhui University, Hefei, 230601, China

²Anhui Key Laboratory of Information Materials and Devices, Hefei, 230601, China

³Institute of Physical Science and Information Technology, Anhui University, Hefei, 230601, China

*Corresponding Author: Guang Li. Email: liguang1971@ahu.edu.cn

Received: 16 November 2019; Accepted: 19 February 2020

Abstract: A novel sunflower-like nanocomposite of SrCo_2S_4 nanoflakes and functionalized multiwall carbon nanotubes (f-MWCNTs) entanglement enveloped in nitrogen-reduced graphene oxide (N-RGO) is prepared by a cheap process. The unique entanglement structure of the material exhibits higher specific surface area, better electrical conductivity and other properties. This helps to reduce the transfer resistance in the photoelectric process of the battery and improve the electrochemical activity, thus increasing the photoelectric conversion efficiency of the battery. The new ternary cobalt-based sulfide material can replace platinum as the counter electrode (CE) material loaded on dye-sensitized solar cells (DSSCs). DSSCs with SrCo_2S_4 @f-MWCNTs@N-RGO (SCS@f-M@N-R) as CE material show excellent photoelectric conversion efficiency (PCE, 8.06%), even surpassing than that of Pt CE material (7.51%). The low cost, excellent electrocatalytic performance and simple preparation method of SCS@f-M@N-R nanomaterial provide feasibility for replacing platinum material as the CE material of DSSCs, which is of great significance and persuasion.

Keywords: Dye-sensitized solar cells; sunflower-like; multiwall carbon nanotubes; SrCo_2S_4 ; counter electrode

1 Introduction

The latest research shows that DSSCs are clean, convenient and cheap energy conversion devices that are generating a wide range of interest around the world [1,2]. The main effect of the CE in DSSCs is to transfer negative charges from the photoanode to the I_3^- in the electrolyte, and catalyze the reduction and regeneration of I_3^- . For classical construction, there is else two modules in DSSC; one is a dye-loaded TiO_2 photoanode, the other is a kind of Γ/I_3^- redox electrolyte [3–6]. As we all know, the platinum (Pt) is a sort of excellent CE electrocatalytic material for DSSCs because its conductivity, stability and electrocatalytic performance are all splendid [7–10].

Nevertheless, the low quantity, high cost and much demand in other industrial manufacture of platinum limit its application in DSSCs extensively [11,12]. Therefore, the research of an alternative to platinum



This work is licensed under a Creative Commons Attribution 4.0 International License, which permits unrestricted use, distribution, and reproduction in any medium, provided the original work is properly cited.

electrocatalytic materials becomes critical at this era, which must be economical, stable and effective [13–17]. In recent years of study, metal carbides, metallic oxides, metal sulfides and ternary compounds have come into the view of researchers gradually. Some recent works report that such as Co_3S_4 , Fe_3O_4 , NiMoS_4 , and CuCo_2S_4 nanoparticle materials are good alternatives to platinum as CE in DSSCs [18].

The ternary chalcogenides have two different cations in the single crystal structure, which have abundant redox reactions and broad prospects in the field of DSSC-CE research [19,20]. Cobalt-based ternary sulfide materials, such as NiCo_2S_4 , CuCo_2S_4 , ZnCo_2S_4 , have attracted a lot of attentions due to the popular price and splendid electrochemical property [21,22]. Therefore, SrCo_2S_4 nanoparticles can be used as CE material due to their sterling stability and lasting performance. But, owing to the semiconductor function, SrCo_2S_4 incarnates the fewer catalytic reductions behavior and poor electrical conductivity for I_3^- ion. So, different treatments are needed to improve the property of the CE based on the material of the SrCo_2S_4 nanoparticles, while the PCE of the pure SrCo_2S_4 nanoparticles as CE material in DSSCs arrived at 5.37% in this experiment.

In recent decades, carbon materials have been widely used and their structures have become more and more novel [23]. A number of techniques have been utilized for fabrication of the carbon nanomaterials based composites [24,25]. In particular, mussel-inspired chemistry has been shown to have great potential in the manufacture of a variety of composite materials [26,27]. Inspired by mussel-inspired chemistry, an valid technique for enhancing dispersibility and electrical conductivity of materials is to use carbon support materials [28]. Multiwall carbon nanotubes (MWCNTs) are used as an admirable support material in the fabrication of electrocatalytic materials with excellent performance because of the large specific surface area and excellent stability and conductivity [29]. Compared with other carbon materials, MWCNTs have distinct hollow structure and circumvolute network, which contributes to produce vast bonding points and move the ions in electrolyte [30,31]. The properties of ternary metal sulfide-based nanocomposites with MWCNTs are indeed better than those of original ternary metal sulfide. The following criteria can be used to effectively prepare high-property CE materials in DSSC: splendid conductivity and stability and a lot of active sites for catalytic process [32,33]. However, because of the small size and easy aggregation of SrCo_2S_4 nanoparticles, the rapid movement of electrons between SrCo_2S_4 nanoparticles is delayed. Previous studies have shown that the active points of nanometer support materials mostly exist in the scaffold structure and hollow structure, which provides ideas for improving the stability of materials and the efficiency of electrocatalysis [34,35].

Meanwhile, the graphene is a peculiar planar structural material; it has good chemical stability and excellent charge-mobility interaction with other molecules. Using a similar method, we can wrap metal sulfides in other carbon materials, amorphous carbon, RGO and N-doped RGO are attractive options, such as $\text{NiCo}_2\text{O}_4@\text{RGO}$, $\text{MoS}_2@\text{N-RGO}$ [1]. We could even use several carbon materials to enhance the electrochemical performance, improve the dispersion ability and increase the catalytic efficiency of the CEs, to improve the photoelectric conversion efficiency. After comparing the electrodes encapsulated with RGO and N-RGO, the researchers found that N-RGO has better electrical conductivity, more abundant active sites and larger specific surface area which could improve the catalytic performance [36]. Therefore, we would like to synthesize $\text{SCS}@f\text{-M}@N\text{-R}$ nanocomposites to approach the photoelectric conversion efficiency of Pt, as shown in Fig. 1.

Our study focused on the transition metal cobalt (Co) ternary sulfides, and we noticed that alkali metal strontium (Sr) compounds in electronic semiconductor devices are widely used, its unique physical and chemical performance let us produce strong interest, so we will use the hydrothermal preparation of porous hollow core spherical SrCo_2S_4 as the original electric catalytic properties of ternary sulfides as the initial reference sample; in order to ensure faster collection and extraction of electrons, using multi-walled carbon nanotubes is a good choice. The synthesized SrCo_2S_4 nano microspheres and functionalized

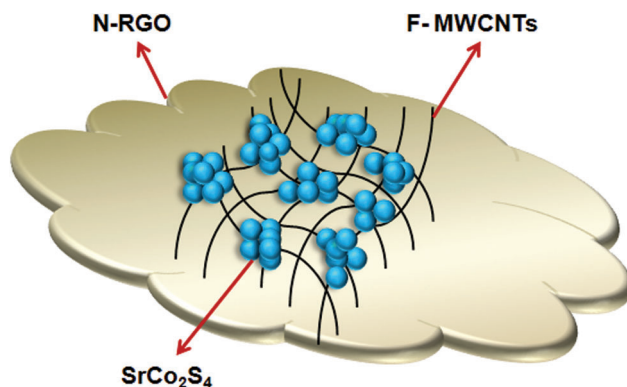


Figure 1: The unique sunflower-like structure of SCS@f-M@N-R

multi-walled carbon nanotubes were heated in ethanol solution to obtain the SCS@f-M nanocomposite, which was taken as the second sample; Sample No. 3 was coated with nitrogen-doped reduced graphite oxide (N-RGO) with less lattice defects to increase the corrosion resistance of the composite material, as shown in Fig. 2.

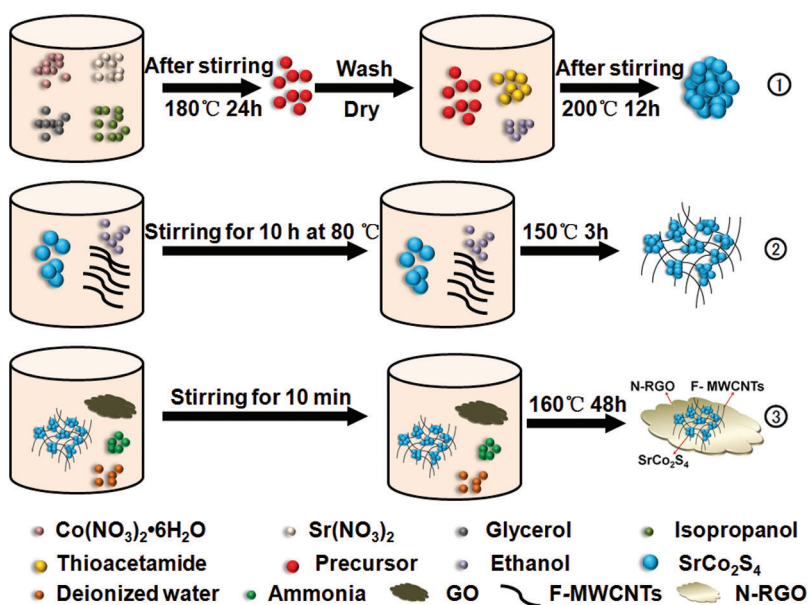


Figure 2: Synthetic route of SrCo₂S₄, SCS@f-M and SCS@f-M@N-R

2 Experiment

2.1 Materials

The cobalt nitrate ((Co(NO₃)₂·6H₂O), strontium nitrate (Sr(NO₃)₂), thioacetamide (CH₃CSNH₂) and polyethylene glycol 20000 (PEG 20000) were purchased from the Tianjin Guangfu Fine Chemical Industry Research Institute. Isopropanol ((CH₃)₂CHOH), glycerol (C₃H₈O₃), sulfuric acid (H₂SO₄), phosphoric acid (H₃PO₄), nitric acid (HNO₃) and ammonium hydroxide (NH₄OH) were bought from Guoyao Chemical Reagent Co., Ltd. Aladdin Reagent Co., Ltd (Shanghai, China) provides iodine redox pairs of confectioned raw materials (LiI, LiClO₄, I₂). Shanghai Mackin Biochemical Co., Ltd. provides

original MWCNTs and graphene oxide (GO) nanosheets. According to the manufacturer's model, the length of MWCNTs is 10–20 μm , the inner diameter is about 5–12 nm, the outer diameter is 25–50 nm, and the purity of MWCNTs is more than 95%. The electrothermal distiller in our laboratory provides deionised water for all experiments.

The Pt covered counter electrode (CE), TiO_2 photoanode, dye N719, electrolyte and fluorine-doped tin oxide (FTO) were provided by Yingkou OPV Tech. New Energy Co., Ltd. Liaoning (Yingkou) China. These electrolytes consist of 0.05M I_2 , 0.5M LiI, 0.5M 4-tert-butylpyridine and 0.6 M1-propyl-2,3-dimethylimidazolium iodide in acetonitrile solution according to the manufacturer's instruction.

2.2 Functionalized Processing of Multiwall Carbon Nanotubes

The purity of MWCNTs purchased from manufacturers is not more than 95%. Therefore, the purity must be improved by removing carbon material particles and metals (such as nickel, cobalt and iron) in the reflux process. The acid treatment of MWCNTs by refluxing process is a simple method to remove impurities and increase the content of $-\text{OH}$ and $-\text{COOH}$ [37]. Usually, 300 mg of original MWCNTs were poured into 100 ml hydrochloric acid (HCl, con. 36.5%) contained by a 200 ml beaker, after 30 minutes of ultrasound, the solution was added to 300 ml three-necked flask. It was cooled naturally at room temperature, centrifuged after a 4h-reflux at 80–90°C, and the supernatant was separated through a decanting method. Then, the precipitated solution was filtered by 0.22 μm polytetrafluoroethylene (PTFE) membrane and washed with water for several times by vacuum filter extractor until the pH reached 7. Then, we dry the residue by using a vacuum freeze dryer at -75°C for 12 hours for subsequent application. Similarly, 150 mg acidified MWCNTs were poured into 100 ml nitric acid (HNO_3 , con. 63%) contained by a 200 ml beaker. After 30 minutes of the liquid ultrasound, the mixture was transferred to a 300 ml three-necked flask, stirred magnetically at 150°C for 6 hours in a reflux operation, and then filtered to extract the sediment. They were eventually dried for 12 hours in a vacuum freeze-dryer at -75°C to obtain MWCNTs rich in the $-\text{COOH}$ group, which were then stored in sealed shade vials for later use.

2.3 Synthesis of Hollow SrCo_2S_4 Nanospheres and SrCo_2S_4 @f-M Nanocomposite

In the common synthesis path of ternary sulfides, a transparent pink solution was obtained by dissolving 0.1456 g of $\text{Co}(\text{NO}_3)_2 \cdot 6\text{H}_2\text{O}$ and 0.0529 g of $\text{Sr}(\text{NO}_3)_2$ in a mixture of isopropanol (70 ml) and glycerol (10 ml). The pink mixed solution was then in a reaction at 180°C for 24 hours through a high pressure closed PTFE autoclave. Purple sediment was obtained by centrifugation after cooling to normal temperature. Then, it was washed 6 times with ethanol and then dried at 60°C. To prepare hollow SrCo_2S_4 nanospheres, dissolved and stirred 0.0500 g thioacetamide (TAA) and 0.0300 g precipitate with 25.0 ml ethanol. At 200°C, the reaction was then sealed in a PTFE autoclave and heated for 12 hours. After several rinses by using centrifugal with distilled water and ethanol, then drying, the hollow SrCo_2S_4 nanospheres were finally acquired. Next, the 0.1g SrCo_2S_4 nanospheres were ultrasonic for 1 h with 30ml ethanol, and the 0.05 g f-MWCNTs was ultrasonic for 1 h with 60 ml ethanol. Next, the SrCo_2S_4 solution was poured into the another solution under ultrasonication for 0.5 h. Then, the ultrasonic mixture was stirred at 80°C for 10 hours and then poured into the PTFE autoclave. After 3 hours of the sealed reaction at 150°C, the precipitate was treated in the same way as mentioned above. Finally, the black precipitate after washing was dried in the vacuum freeze dryer at -75°C for 24 hours and stored for subsequent use.

2.4 Preparation of SCS@f-M@N-R

The synthesis method of N-RGO is as follows: dissolve 30 mg GO in 30 ml deionized water and ultrasonic treatment for 1 hour. Next, we added 3 ml of ammonia and stir for 10 minutes. The mixture was poured into the closed autoclave of PTFE and then baked at 160°C for 48 hours. The resulting mixture was filtered, centrifuged, washed, dried and stored. Then, SCS@f-M@N-R nanocomposites were

synthesized through surface hydrothermal method. SCS@f-M nanocomposites and N-RGO are used as matrix materials in aqueous solutions. Initially, N-RGO (0.03 g) and SCS@f-M (0.09 g) was respectively dispersed in 30 ml water and ultrasonication for 1 hour. Then, the latter solution was poured into the N-RGO solution and maintained further ultrasound treatment within 20–30 minutes to make a homogenous solution. After that, the mixed solution was moved to PTFE autoclave and baked at 120°C for 3 hours. Next, the black liquor was cleaned with water and ethanol for several times. At last the residue was lyophilized in a freeze-dryer with vacuum at -75°C overnight.

2.5 Fabrication of the CEs Based on DSSC

The prepared samples are regarded as original materials for the manufacture of CEs. Typically, we grind 0.01 g of polyethylene glycol (PEG20000) with 0.04 g of composite material, which is a ratio of 1 to 4, in a small amount of alcohol until a thick black slurry is formed. For this reason, the FTO laminated glass substrate was needed. Clean the cut FTO with deionized water, and after three or four times of ultrasonic treatment with ethanol, put it in the oven to dry. A digital multimeter (DMM) is used to measure the conducting surface of the dried FTO. Tape (3 M) is affixed to both sides of the wide edge of the conducting surface. Use a scraper to evenly spread the thick grinding fluid between the tapes and form a film with an area of 0.5 cm × 0.5 cm. Once the film has dried, remove the tape from the sides of the FTO. Finally, the CEs were annealed in a 400°C tube furnace in Ar atmosphere for 4 hours. DSSC is usually fabricated by assembling a titanium dioxide photoelectric anode (dye-sensitized) and a prepared CE escorted by adding redox electrolyte. Initially, the purchased titanium dioxide photocatalyst with a surface area of 0.4 cm × 0.4 cm was sensitized by immersing dye solution in darkness at 25°C for 20 hours. After that, the sensitized titanium dioxide photocatalyst was cleaned with alcohol and dry slowly with a hair dryer. Titanium dioxide photocathode and counter electrode were separated with transparent tape. Finally, we filled the space between the two electrodes with acetonitrile electrolyte.

2.6 Testing Method

In our study, the X-ray diffraction (XRD) pattern of the sample was measured using the Japanese X-ray diffractometer Rigaku/MAX-3A “CuK_α radiation source ($\lambda = 1.54056 \text{ \AA}$).” The parameters were set in the 2θ angle range of 10°–80° scanned at 4°/min. Transmission electron microscopy (TEM) and scanning electron microscopy (SEM) can provide the microstructure image of the samples. Raman spectroscopy can prove the presence of a large amount of carbon on the surface of the samples. X-ray photoelectron spectroscopy (XPS) can be used to determine the types and approximate proportions of elements on the surface of the sample. The catalytic properties of the CE coated with samples can be obtained by cyclic voltammetry in a three-electrode system connected to an electrochemical workstation (ZAHNERZENNIUM CIMPS-1, Germany). Similarly, the electrochemical workstation can also measure the Tafel polarization curves and electrochemical impedance spectroscopy (EIS) of the CE coated with samples. When the condition of illumination was AM 1.5 and 100 mW cm⁻², the photoelectric current density voltage ($J-V$) curve was measured with a digital source meter (Keithley 2410).

3 Test Results of Each Part

3.1 Morphological Structure and Elemental Composition

The XRD result of the SrCo₂S₄, SCS@f-M, SCS@f-M@N-R are revealed in Fig. 3, all the diffraction peaks of SrCo₂S₄ occurring at 15.0°, 16.2°, 17.8°, 20.2°, 22.1°, 24.8°, 30.9° could be matched to (110), (002), (200), (112), (211), (202), (220) plane of standard card (JCPDS 73-1180), obviously, the main diffraction peak of SrCo₂S₄ is at 22.1°. Moreover, the increase of the width of the diffraction peak of SCS@f-M@N-R indicates that the SrCo₂S₄ nanoparticles are very small and uniformly spread across the surface of N-RGO; the disappearance of the peak of SCS@f-M indicates that the hollow spherical SrCo₂S₄ decomposes gradually under the action of carbon nanotubes and forms a disorderly entangled structure.

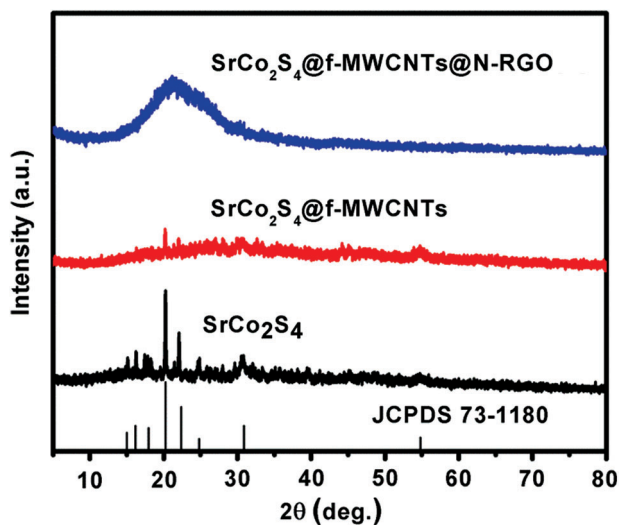


Figure 3: X-ray diffraction patterns of SrCo_2S_4 , SCS@f-M and SCS@f-M@N-R nanoparticles

The surface morphologies and microstructures of the all materials were provided by SEM and TEM. In Figs. 4a and 4b, the samples of SrCo_2S_4 synthesized by hydrothermal method show hollow spherical shape with a radius of about 200 nm, and the surface particles are arranged tightly. In Fig. 4c, under the catalysis of functionalized multiwall carbon nanotubes, hollow spherical samples were decomposed into flaky powders. Furthermore, the flake sample was combined with f-MWCNTs to form a sunflower-like shape compound, and they come together in the shape of a bird's nest. Next, we can see the entangled products of the above synthesis are evenly wrapped on the thin film of N-RGO in Fig. 4d. HR-TEM images of some typical regions in the SCS@f-M@N-R sample can be observed in Figs. 4e and 4f. The two images expose that the visible lattice spacing of SrCo_2S_4 of 0.19 nm can match with crystal face (220) of SrCo_2S_4 , which is matched with the result of XRD. As shown in the pictures of TEM, the entangled network structure of the sample with MWCNTs has a larger specific surface area, which is helpful to the I_3^- diffusion and the availability of redox coupling points in electrolytes.

Raman spectra result of SrCo_2S_4 , SCS@f-M , SCS@f-M@N-R are showed in Fig. 5. From this picture, two strong peaks at about 1348.5 cm^{-1} and 1583.5 cm^{-1} of the samples are presented, which are respectively distributed to the disordered and graphene band [38]. The peaks at band D showed the disorder and defect in the structure of GO, while those at band G showed the vibration mode corresponding to the Sp^2 bond in the hexagonal structure of two-dimensional grapheme [39]. These show that the SCS@f-M nano-conjugates are well wrapped in the N-RGO layer, which is similar to the result of XRD analysis.

The XPS measurements further analyze the elemental composition in the surface of the hybrid material [40,41]. The element approximate proportions calculated from the XPS test are shown in Tab. 1. We can see that the content of Sr element on the surface of the sample is low, and the content of S and Co element decreases with the addition of the carbon material, and N element is successfully doped into RGO. The measurement scanning spectrum in Figs. 6 and 7 proves the presence of N 1s, O 1s, C 1s, S 2p, Sr 3d and Co 2p signals, demonstrating the presence of nitrogen, oxygen, carbon, sulfur, strontium and cobalt elements in the composite material. And the N 1s peak in the result of SCS@f-M@N-R was compared with SrCo_2S_4 and SCS@f-M , which confirmed the success of nitrogen doping [42]. The test of X-ray photoelectron spectroscopy shows that the experiment successfully obtains the SCS@f-M@N-R nanocomposites.

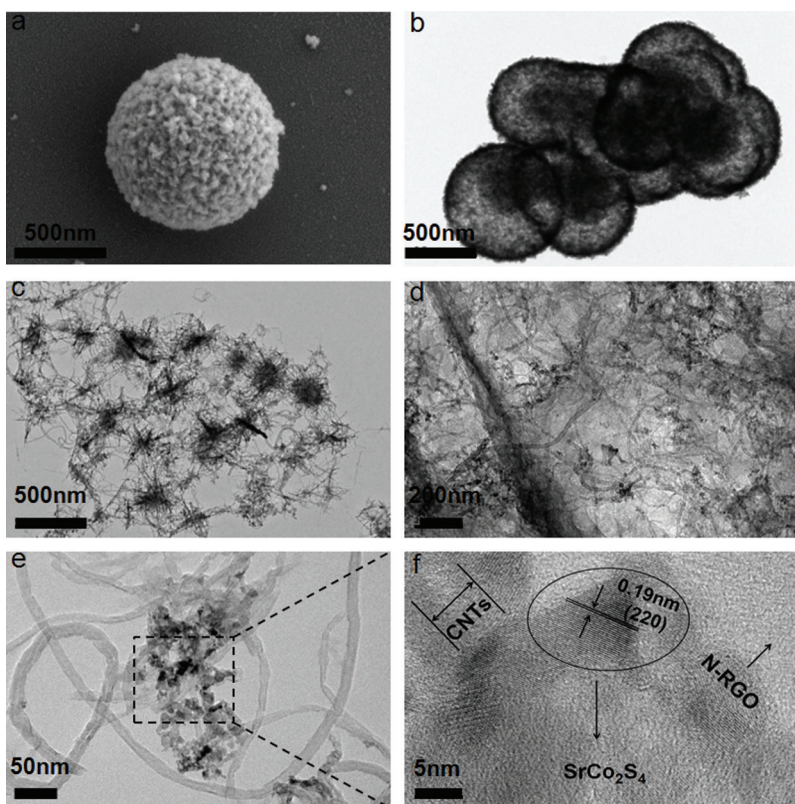


Figure 4: (a) SEM image of SrCo_2S_4 nano flake (b) TEM image of SrCo_2S_4 nano flakes (c) TEM image of SCS@f-M with tangled structure (d) TEM image of SCS@f-M covered with N-RGO (e) TEM image of SCS@f-M@N-R (f) The image of SCS@f-M@N-R in HR-TEM

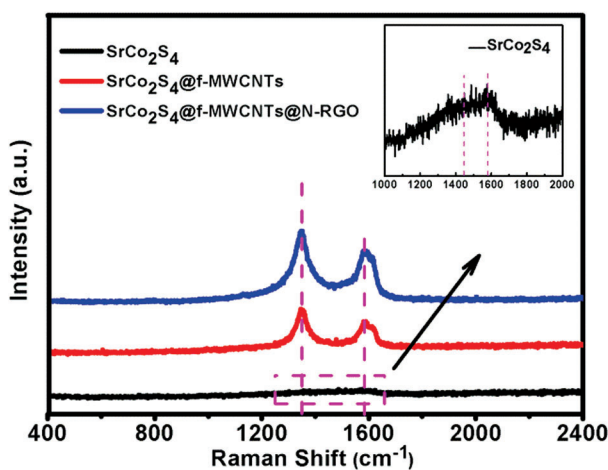


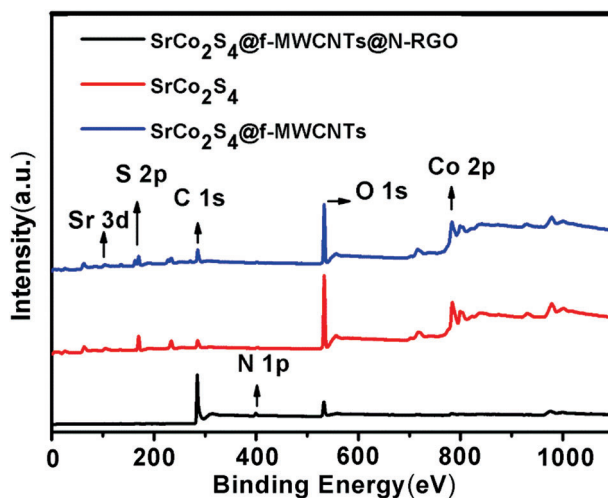
Figure 5: Raman spectra of SrCo_2S_4 , SCS@f-M and SCS@f-M@N-R nanoparticles in the wavelength range of 200–2500 cm^{-1}

3.2 Cyclic Voltammetry Analysis

The cyclic voltammetry (CV) curve of the sample can be measured by the three-electrode system, and the electrocatalytic performance of the sample can be analyzed. Fig. 8a indicates that the CV curves of Pt,

Table 1: The proportion of different elements on the surface of each sample

CE materials	Sr	Co	S	C	O	N
SrCo ₂ S ₄	0.19%	51.73%	48.08%	0	0	0
SCS@f-M	1.30%	26.22%	37.86%	34.61%	0	0
SCS@f-M@N-R	0.06%	1.05%	1.30%	70.15%	21.41%	6.02%

**Figure 6:** “X-ray photoelectron spectroscopy (XPS)” survey spectra of SrCo₂S₄, SCS@f-M and SCS@f-M@N-R nanoparticles

SrCo₂S₄, SCS@f-M, SCS@f-M@N-R electrode in I₃⁻/I⁻ electrolyte system. As we can see, the oxidation peak of SCS@f-M@N-R CE is higher than that of Pt CE, while the reduction peak is lower. In addition, the interval of SCS@f-M@N-R CE between oxidation peak to reduction peak (ΔE_{pp}) is about 0.29 V, which is the smallest among all the electrode materials tested (Tab. 2). The results show that SCS@f-M@N-R CE has better electrocatalytic activity, lower over potential and faster reaction speed, which is due to the sunflower-like shape. In this entangled structure of SCS@f-M@N-R, the concentrated SrCo₂S₄ mainly play a catalytic role; the f-MWCNTs mainly play the role of fast electron collection and transmission, while increasing the specific surface area; N-RGO is responsible for protecting internally catalytic active substances from electrolyte corrosion [43,44]. Also, electrochemical stability is an another key index for the CE. From the Fig. 8b, we can observe that the peaks of the cyclic voltammetry curve of SCS@f-M@N-R, which has been tested for 10 times, basically coincide, with no deviation and no attenuation.

3.3 Electrochemical Impedance Spectroscopy Analysis

Electrochemical impedance spectroscopy (EIS) can reflect the charge-transfer characteristics of direct current circuits. EIS studies have been widely used to explore negative ions on the reduced reverse electrode of I₃⁻, as well as well-loaded equivalent circuits. The R_s values indicate the range of similar series resistances formed by the electrolyte and electrode, while the R_{ct} values reveal the charge transfer resistance at the CE/electrolyte interface. In the Nyquist curves of EIS, the first semicircle is located in the high-frequency region and represents the value of R_s . The second semicircle and the last tail represent the low-frequency region, which correspondingly describes the charge transfer (R_{ct}) at the interface between TiO₂/N719/electrolyte and the value of the Nernst diffusion impedance (Z_N) [45–47]. In Fig. 9a,

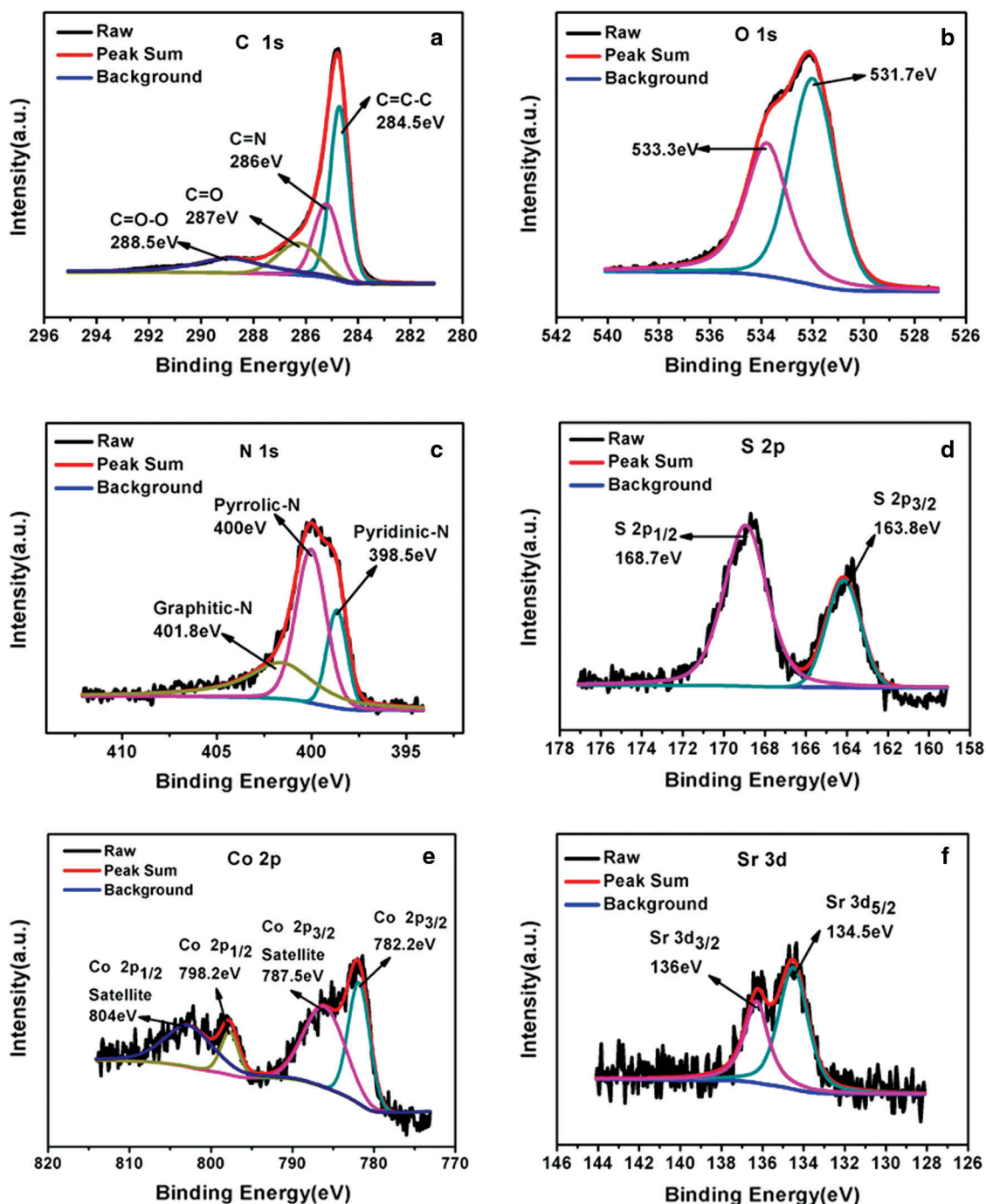


Figure 7: (a) C 1s XPS spectrum of SrCo₂S₄@fMWCNTs@N-RGO (b) O 1s XPS spectrum of SCS@f-M@N-R (c) N 1s XPS spectrum of SCS@f-M@N-R (d) S 2p XPS spectrum of SCS@f-M@N-R (e) Co 2p XPS spectrum of SCS@f-M@N-R (f) Sr 2p XPS spectrum of SCS@f-M@N-R

the R_{ct} of the Pt, SrCo₂S₄, SCS@f-M and SCS@f-M@N-R electrodes are about 0.30, 2.09, 0.41 and 0.26 Ω cm² respectively, which is summarized in Tab. 2. SCS@f-M@N-R has a reduced R_{ct} value, which indicates that there are higher conductivity and a even bigger specific surface area in the nanocomposite with sunflower-like entangled structure, thus improving the electrochemical efficiency of the counter electrode of DSSC [48–52].

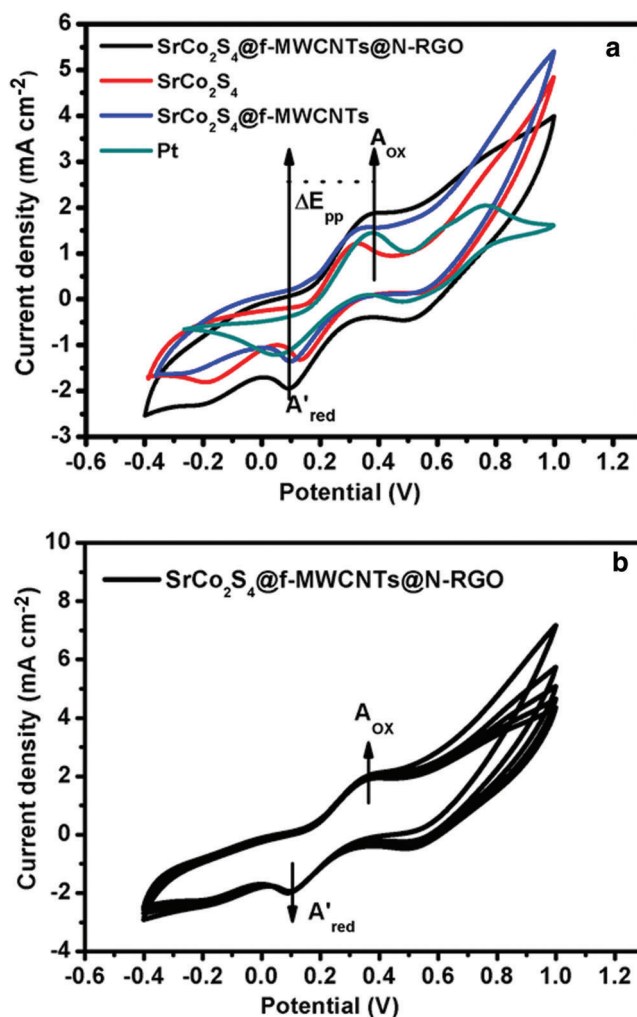


Figure 8: (a) CV curves for Pt, SrCo₂S₄, SCS@f-M and SCS@f-M@N-R counter electrodes (b) CV curves of SCS@f-M@N-R with 20 cycles successive scans

Table 2: CV, EIS and Tafel polarization parameters based on different CE materials in DSSC obtained from Figs. 8 and 9

CE materials	R_s (Ω cm ²)	R_{ct} (Ω cm ²)	$\lg J_0$ (mA cm ⁻²)	$\lg J_{lim}$ (mA cm ⁻²)	ΔE_{pp} (V)
Pt	6.06 ± 0.01	0.30 ± 0.01	1.63 ± 0.01	2.08 ± 0.01	0.32 ± 0.01
SrCo ₂ S ₄	7.79 ± 0.01	2.09 ± 0.01	0.78 ± 0.01	2.01 ± 0.01	0.49 ± 0.01
SCS@f-M	5.70 ± 0.01	0.41 ± 0.01	1.50 ± 0.01	2.36 ± 0.01	0.23 ± 0.01
SCS@f-M@N-R	5.73 ± 0.01	0.26 ± 0.01	1.69 ± 0.01	2.65 ± 0.01	0.29 ± 0.01

3.4 Tafel Polarization Analysis

Using the platinum electrode as a control, we can observe the charge diffusion and transfer characteristics on the surface of CE and the catalytic activity of Γ/I_3^- redox pairs from the measured Tafel polarization curve. The exchange current density (J_0) in Fig. 9b is calculated from the specific slope on the Tafel curve, and the limit current density (J_{lim}) is equal to the Y-axis value of the intersection point of

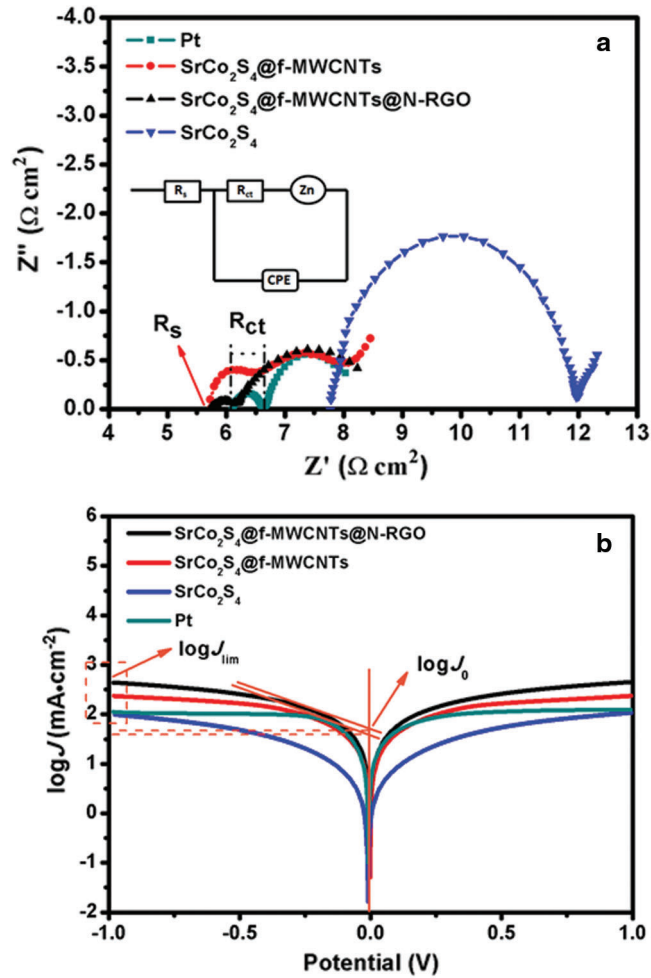


Figure 9: (a) Electrochemical impedance spectra of the CEs (b) Tafel polarization curves of the CEs

the cathode branch and the Y-axis [53–55]. From Fig. 9b, we can find that the J_0 value relation of the all four CEs is SCS@f-M@N-R > Pt > SCS@f-M > SrCo₂S₄, while the J_{lim} value relation is SCS@f-M@N-R > SCS@f-M > Pt > SrCo₂S₄ (Tab. 2). Through the analysis of Tafel curve, the parameters J_0 and J_{lim} between electrolyte and electrode material are obtained, which can also be calculated from the Eqs. (1) and (2), revealing the catalytic activity and efficiency between electrolyte and electrode material.

$$J_0 = \frac{RT}{nFR_{ct}} \quad (1)$$

$$J_{lim} = \frac{2neDCN_A}{d} \quad (2)$$

In Formula (1), T is absolute temperature, R is universal gas constant, R_{ct} is the charge transfer resistance at electrolyte interface, n is the number of stoichiometric electrons participating in the reaction and F is Faraday constant. In Formula (2), D is the coefficient of diffusion triiodide, C is the concentration of triiodide, e is the value of charge, d is electrode distance and N_A is Avogadro's constant [6,51,56–58]. As a result, compared with Pt, the SCS@f-M@N-R has higher catalytic performance, faster electron transmission efficiency and larger diffusion coefficient, which is in coordination with EIS analysis results.

3.5 Photovoltaic Performance Analysis

In the search for an alternative of the Pt CE, the photoelectric performance is not negligible. Fig. 10a shows the photocurrent density-voltage (J - V) curve of the DSSCs loaded with Pt, SrCo₂S₄, SCS@f-M and SCS@f-M@N-R as the counter electrode material. Tab. 3 summarizes the open-circuit photovoltage (V_{oc}), short-circuit photocurrent density (J_{sc}), photoelectric conversion efficiency (PCE), filling factor (FF)

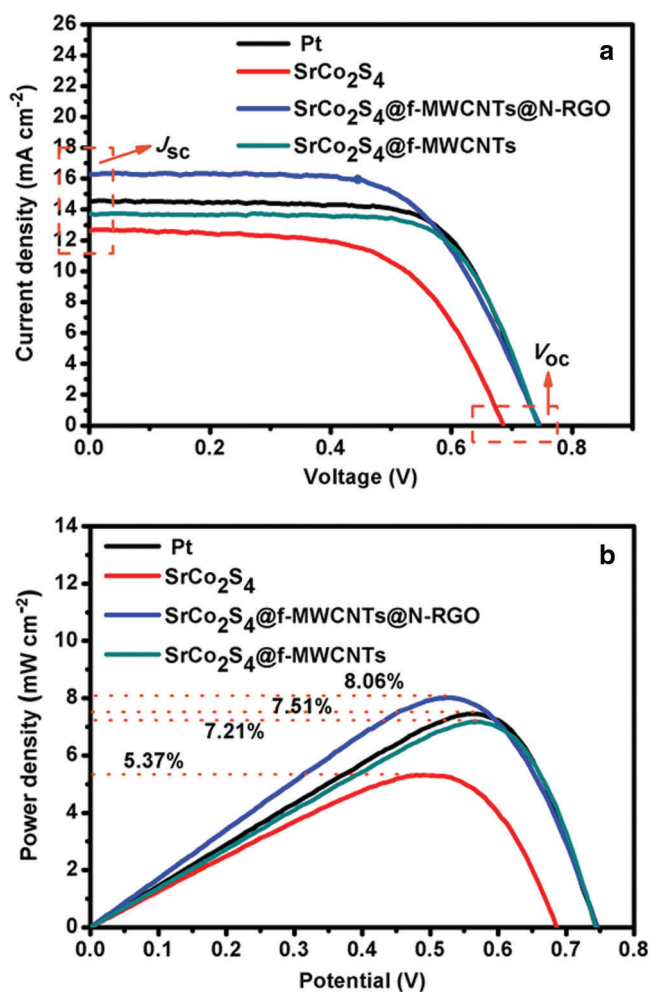


Figure 10: (a) Photoelectric curves of the different DSSCs (b) PCE curves of the different DSSCs

Table 3: Photovoltaic parameters of different CEs based in DSSCs

CE materials	J_{sc} (mA cm ⁻²)	V_{oc} (V)	FF (%)	PCE (%)
Pt	14.588	0.742	68.092	7.51
SrCo ₂ S ₄	12.684	0.685	60.083	5.37
SCS@f-M	13.715	0.743	65.555	7.21
SCS@f-M@N-R	16.322	0.745	70.197	8.06

gained from the Fig. 10. According to the Tab. 3, the DSSC based on SCS@f-M@N-R as the CE can reach 0.745V in V_{oc} , 70.197% in filling FF, 16.322 mA cm⁻² in J_{sc} , 8.06% in PCE. This shows that the excellent photovoltaic performance of SCS@f-M@N-R far exceeds that of pure SrCo₂S₄. Moreover, the photoelectric conversion efficiency of SCS@f-M@N-R exceeds the performance of Pt (7.51%), which makes the nanomaterial could replace Pt, which has been reflected in the previous studies.

4 Conclusions

To sum up, when SrCo₂S₄ hollow sphere nanoparticles prepared by hydrothermal method in the laboratory were directly applied to DSSC, the corresponding PCE was only 5.37%, lower than that of Pt. From the analysis of all above test, we can conclude that the electrocatalytic activity of pure hollow sphere SrCo₂S₄ is weak. However, the hollow sphere structure has a larger specific surface after being broken. So we introduced MWCNTs to forming the tangled and sunflower-like structure of SCS@f-M nanocomposite. This structure allows the retention of a huge specific surface area while improving the performance of other aspects. The wrapping behaviour of N-RGO can enhance the stability of the sample and further improve the electrocatalytic performance. The final nanocomposite has been applied in the counter electrode of DSSC, showing excellent electrocatalytic performance and splendid stability. In the study after the assembly of DSSC, the PCE of SCS@f-M@N-R electrode is higher than the performance of Pt electrode. The low cost, excellent electrocatalytic performance and simple preparation method of SCS@f-M@N-R nanomaterial provide feasibility for replacing platinum material as the CE material of DSSC, which is of great significance and persuasion.

Funding Statement: This work was financially supported by National Natural Science Foundation of China (11674001), National Key R&D Program of China (2017YFA0403503), Open fund for Discipline Construction, Anhui Provincial Natural Science Foundation (1708085MA07,1708085QE116), Institute of Physical Science and Information Technology (S01003103, Anhui University), the Doctoral research start-up funds projects of Anhui University (J01003201), and the Key Natural Science Research Program of Anhui Educational Committee (KJ2018ZD001).

Conflicts of Interest: The authors declare that they have no conflicts of interest to report regarding the present study.

References

1. Du, F., Zuo, X., Yang, Q., Yang, B., Li, G. et al. (2016). The stabilization of NiCo₂O₄ nanobelts used for catalyzing triiodides in dye-sensitized solar cells by the presence of RGO sheets. *Solar Energy Materials and Solar Cells*, 149, 9–14. DOI 10.1016/j.solmat.2015.11.025.
2. Zhang, Q., Park, K., Xi, J., Myers, D., Cao, G. (2011). Recent progress in dye-sensitized solar cells using nanocrystallite aggregates. *Advanced Energy Materials*, 1(6), 988–1001. DOI 10.1002/aenm.201100352.
3. Abdullah, H., Atiqah, N. A., Omar, A., Asshaari, I., Mahalingam, S. et al. (2015). Structural, morphological, electrical and electron transport studies in ZnO-rGO (wt% = 0.01, 0.05 and 0.1) based dye-sensitized solar cell. *Journal of Materials Science: Materials in Electronics*, 26(4), 2263–2270. DOI 10.1007/s10854-015-2679-y.
4. Kumar, R. S. S., Grancini, G., Petrozza, A., Abrusci, A., Snaith, H. et al. (2013). Effect of polymer morphology on P3HT-based solid-state dye sensitized solar cells: an ultrafast spectroscopic investigation. *Optics Express*, 21(9), A469–A474. DOI 10.1364/OE.21.00A469.
5. Kim, D. J., Koh, J. K., Lee, C. S., Kim, J. H. (2014). Mesh-shaped nanopatterning of Pt counter electrodes for dye-sensitized solar cells with enhanced light harvesting. *Advanced Energy Materials*, 4(18), 1400414. DOI 10.1002/aenm.201400414.
6. Hauch, A., Georg, A. (2001). Diffusion in the electrolyte and charge-transfer reaction at the platinum electrode in dye-sensitized solar cells. *Electrochimica Acta*, 46(22), 3457–3466. DOI 10.1016/S0013-4686(01)00540-0.

7. Wu, J., Tang, Z., Huang, Y., Huang, M., Yu, H. et al. (2014). A dye-sensitized solar cell based on platinum nanotube counter electrode with efficiency of 9.05%. *Journal of Power Sources*, 257, 84–89. DOI 10.1016/j.jpowsour.2014.01.090.
8. Grätzel, M. (2001). Photoelectrochemical cells. *Nature*, 414(6861), 338–344. DOI 10.1038/35104607.
9. Cui, X., Xiao, J., Wu, Y., Du, P., Si, R. et al. (2016). A graphene composite material with single cobalt active sites: a highly efficient counter electrode for dye-sensitized solar cells. *Angewandte Chemie International Edition*, 55(23), 6708–6712. DOI 10.1002/anie.201602097.
10. Calogero, G., Calandra, P., Irrera, A., Sinopoli, A., Citro, I. et al. (2011). A new type of transparent and low cost counter-electrode based on platinum nanoparticles for dye-sensitized solar cells. *Energy & Environmental Science*, 4(5), 1838–1844. DOI 10.1039/c0ee00463d.
11. Yao, F., Sun, P., Sun, X., Huang, N., Ban, X. et al. (2016). One-step hydrothermal synthesis of ZnS-CoS microcomposite as low cost counter electrode for dye-sensitized solar cells. *Applied Surface Science*, 363, 459–465. DOI 10.1016/j.apsusc.2015.12.036.
12. Wasim Khan, M., Zuo, X., Yang, Q., Tang, H., Rehman, K. M. U. et al. (2020). Quantum dot embedded N-doped functionalized multiwall carbon nanotubes boost the short-circuit current of Ru(ii) based dye-sensitized solar cells. *Nanoscale*, 12(2), 1046–1060. DOI 10.1039/C9NR09227G.
13. Yu, X. Y., Yu, L., Lou, X. W. (2016). Metal sulfide hollow nanostructures for electrochemical energy storage. *Advanced Energy Materials*, 6(3), 1501333. DOI 10.1002/aenm.201501333.
14. Liu, T., Mai, X., Chen, H., Ren, J., Liu, Z. et al. (2018). Carbon nanotube aerogel-CoS₂ hybrid catalytic counter electrodes for enhanced photovoltaic performance dye-sensitized solar cells. *Nanoscale*, 10(9), 4194–4201. DOI 10.1039/C7NR09260A.
15. van Franeker, J. J., Kouijzer, S., Lou, X., Turbiez, M., Wienk, M. M. et al. (2015). Depositing fullerenes in swollen polymer layers via sequential processing of organic solar cells. *Advanced Energy Materials*, 5(14), 1500464. DOI 10.1002/aenm.201500464.
16. Shi, Q., Chen, Z., Song, Z., Li, J., Dong, J. (2011). Synthesis of ZIF-8 and ZIF-67 by steam-assisted conversion and an investigation of their tribological behaviors. *Angewandte Chemie International Edition*, 50(3), 672–675. DOI 10.1002/anie.201004937.
17. Zheng, X., Guo, J., Shi, Y., Xiong, F., Zhang, W. et al. (2013). Low-cost and high-performance CoMoS₄ and NiMoS₄ counter electrodes for dye-sensitized solar cells. *Chemical Communications*, 49(83), 9645–9647. DOI 10.1039/c3cc45064c.
18. Zhang, Z., Chen, G., Wang, H., Li, X. (2015). Template-directed in situ polymerization preparation of nanocomposites of PEDOT: PSS-coated multi-walled carbon nanotubes with enhanced thermoelectric property. *Chemistry—An Asian Journal*, 10(1), 149–153. DOI 10.1002/asia.201403100.
19. An, C., Wang, Y., Huang, Y., Xu, Y., Jiao, L. et al. (2014). Porous NiCo₂O₄ nanostructures for high performance supercapacitors via a microemulsion technique. *Nano Energy*, 10, 125–134. DOI 10.1016/j.nanoen.2014.09.015.
20. Deng, F., Yu, L., Cheng, G., Lin, T., Sun, M. et al. (2014). Synthesis of ultrathin mesoporous NiCo₂O₄ nanosheets on carbon fiber paper as integrated high-performance electrodes for supercapacitors. *Journal of Power Sources*, 251, 202–207. DOI 10.1016/j.jpowsour.2013.11.048.
21. Xiao, J., Wan, L., Yang, S., Xiao, F., Wang, S. (2014). Design hierarchical electrodes with highly conductive NiCo₂S₄ nanotube arrays grown on carbon fiber paper for high-performance pseudocapacitors. *Nano Letters*, 14(2), 831–838. DOI 10.1021/nl404199v.
22. Zou, R., Zhang, Z., Yuen, M. F., Hu, J., Lee, C. S. et al. (2015). Dendritic heterojunction nanowire arrays for high-performance supercapacitors. *Scientific Reports*, 5(1), 7862. DOI 10.1038/srep07862.
23. Snowdon, M. R., Mohanty, A. K., Misra, M. (2017). Examination of a biobased carbon nucleating agent on poly (lactic acid) crystallization. *Journal of Renewable Materials*, 5(1), 94–105. DOI 10.7569/JRM.2017.634134.
24. Dai, L., Li, Y. T., Liu, R., Si, C. L., Ni, Y. H. (2019). Green mussel-inspired lignin magnetic nanoparticles with high adsorptive capacity and environmental friendliness for chromium (III) removal. *International Journal of Biological Macromolecules*, 132, 478–486. DOI 10.1016/j.ijbiomac.2019.03.222.

25. Huang, Q., Zhao, J., Liu, M., Chen, J., Zhu, X. et al. (2018). Preparation of polyethylene polyamine@tannic acid encapsulated MgAl-layered double hydroxide for the efficient removal of copper (II) ions from aqueous solution. *Journal of the Taiwan Institute of Chemical Engineers*, 82, 92–101. DOI 10.1016/j.jtice.2017.10.019.
26. Zeng, G., Huang, L., Huang, Q., Liu, M., Xu, D. et al. (2018). Rapid synthesis of MoS₂-PDA-Ag nanocomposites as heterogeneous catalysts and antimicrobial agents via microwave irradiation. *Applied Surface Science*, 459, 588–595. DOI 10.1016/j.apsusc.2018.07.144.
27. Shi, Y., Liu, M., Deng, F., Zeng, G., Wan, Q. et al. (2017). Recent progress and development on polymeric nanomaterials for photothermal therapy: a brief overview. *Journal of Materials Chemistry B*, 5(2), 194–206. DOI 10.1039/C6TB02249A.
28. Liu, Y., Huang, H. Y., Gan, D. F., Guo, L. R., Liu, M. Y. et al. (2018). A facile strategy for preparation of magnetic graphene oxide composites and their potential for environmental adsorption. *Ceramics International*, 44(15), 18571–18577. DOI 10.1016/j.ceramint.2018.07.081.
29. Moysowicz, A., Śliwak, A., Gryglewicz, G. (2016). Influence of structural and textural parameters of carbon nanofibers on their capacitive behavior. *Journal of Materials Science*, 51(7), 3431–3439. DOI 10.1007/s10853-015-9660-2.
30. Montagna, L. S., Oyama, I. C., Lamparelli, R., Silva, A. P., Montanheiro, T. L. D. et al. (2019). Evaluation of biodegradation in aqueous medium of poly(hydroxybutyrate-co-hydroxyvalerate)/carbon nanotubes films in respirometric system. *Journal of Renewable Materials*, 7(2), 117–128. DOI 10.32604/jrm.2019.00036.
31. Tang, W., Hou, Y., Wang, X., Bai, Y., Zhu, Y. et al. (2012). A hybrid of MnO₂ nanowires and MWCNTs as cathode of excellent rate capability for supercapacitors. *Journal of Power Sources*, 197, 330–333. DOI 10.1016/j.jpowsour.2011.09.050.
32. Yang, B., Zuo, X., Chen, P., Zhou, L., Yang, X. et al. (2015). Nanocomposite of tin sulfide nanoparticles with reduced graphene oxide in high-efficiency dye-sensitized solar cells. *ACS Applied Materials & Interfaces*, 7(1), 137–143. DOI 10.1021/am5040522.
33. Gu, W., Hu, L., Hong, W., Jia, X., Li, J. et al. (2016). Noble-metal-free Co₃S₄/S/G porous hybrids as an efficient electrocatalyst for oxygen reduction reaction. *Chemical Science*, 7(7), 4167–4173. DOI 10.1039/C6SC00357E.
34. Akhtar, M. S. (2017). Ni-Co bimetallic nanoparticles anchored reduced graphene oxide as an efficient counter electrode for the application of dye sensitized solar cells. *Journal of Materials Science: Materials in Electronics*, 28(1), 823–831. DOI 10.1007/s10854-016-5596-9.
35. Zhang, Y. F., Hou, W. S., Guo, H., Shi, S., Dai, J. M. (2019). Preparation and characterization of carbon microspheres from waste cotton textiles by hydrothermal carbonization. *Journal of Renewable Materials*, 7(12), 1309–1319. DOI 10.32604/jrm.2019.07884.
36. Ghasemi, S., Hosseini, S. R., Kazemi, Z. (2018). Electrophoretic preparation of graphene-iron oxide nanocomposite as an efficient Pt-free counter electrode for dye-sensitized solar cell. *Journal of Solid State Electrochemistry*, 22(1), 245–253. DOI 10.1007/s10008-017-3741-x.
37. Hamilton, R. F. Jr., Xiang, C., Li, M., Ka, I., Yang, F. et al. (2013). Purification and sidewall functionalization of multiwalled carbon nanotubes and resulting bioactivity in two macrophage models. *Inhalation Toxicology*, 25(4), 199–210. DOI 10.3109/08958378.2013.775197.
38. Hsieh, C. T., Lin, Y. T., Chen, W. Y., Wei, J. L. (2009). Parameter setting on growth of carbon nanotubes over transition metal/alumina catalysts in a fluidized bed reactor. *Powder Technology*, 192(1), 16–22. DOI 10.1016/j.powtec.2008.11.004.
39. Jiménez, J. A., Sendova, M., Sendova-Vassileva, M. (2011). Real-time monitoring of plasmonic evolution in thick Ag: SiO₂ films: nanocomposite optical tuning. *ACS Applied Materials & Interfaces*, 3(2), 447–454. DOI 10.1021/am101021a.
40. Shutthanandan, V., Nandasiri, M., Zheng, J., Engelhard, M. H., Xu, W. et al. (2019). Applications of XPS in the characterization of Battery materials. *Journal of Electron Spectroscopy and Related Phenomena*, 231, 2–10. DOI 10.1016/j.elspec.2018.05.005.

41. Moulder, J. F. (2019). The impact of the scanning XPS microprobe on industrial applications of X-ray photoelectron spectroscopy. *Journal of Electron Spectroscopy and Related Phenomena*, 231, 43–49. DOI 10.1016/j.elspec.2018.04.003.
42. Chang, C. W., Hu, C. (2020). Graphene oxide-derived carbon-doped SrTiO₃ for highly efficient photocatalytic degradation of organic pollutants under visible light irradiation. *Chemical Engineering Journal*, 383, 123116. DOI 10.1016/j.cej.2019.123116.
43. Yao, R. Y., Zhou, Z. J., Hou, Z. L., Wang, X., Zhou, W. H. et al. (2013). Surfactant-free CuInS₂ nanocrystals: an alternative counter-electrode material for dye-sensitized solar cells. *ACS Applied Materials & Interfaces*, 5(8), 3143–3148. DOI 10.1021/am400031w.
44. Li, B., Wang, L., Kang, B., Wang, P., Qiu, Y. (2006). Review of recent progress in solid-state dye-sensitized solar cells. *Solar Energy Materials and Solar Cells*, 90(5), 549–573. DOI 10.1016/j.solmat.2005.04.039.
45. Li, G. R., Wang, F., Jiang, Q. W., Gao, X. P., Shen, P. W. (2010). Carbon nanotubes with titanium nitride as a low-cost counter-electrode material for dye-sensitized solar cells. *Angewandte Chemie International Edition*, 49(21), 3653–3656. DOI 10.1002/anie.201000659.
46. Yang, H. G., Zeng, H. C. (2004). Self-construction of hollow SnO₂ octahedra based on two-dimensional aggregation of nanocrystallites. *Angewandte Chemie International Edition*, 43(44), 5930–5933. DOI 10.1002/anie.200461129.
47. Gong, F., Wang, H., Xu, X., Zhou, G., Wang, Z. S. (2012). In situ growth of Co₀. 85Se and Ni₀ 85Se on conductive substrates as high-performance counter electrodes for dye-sensitized solar cells. *Journal of the American Chemical Society*, 134(26), 10953–10958.
48. Xue, Y., Liu, J., Chen, H., Wang, R., Li, D. et al. (2012). Nitrogen-doped graphene foams as metal-free counter electrodes in high-performance dye-sensitized solar cells. *Angewandte Chemie International Edition*, 51(48), 12124–12127. DOI 10.1002/anie.201207277.
49. Jiao, Y., Zheng, Y., Davey, K., Qiao, S. Z. (2016). Activity origin and catalyst design principles for electrocatalytic hydrogen evolution on heteroatom-doped graphene. *Nature Energy*, 1(10), 16130. DOI 10.1038/nenergy.2016.130.
50. Xu, J., Zhao, Y., Shen, C., Guan, L. (2013). Sulfur-and nitrogen-doped, ferrocene-derived mesoporous carbons with efficient electrochemical reduction of oxygen. *ACS Applied Materials & Interfaces*, 5(23), 12594–12601. DOI 10.1021/am4039294.
51. Yu, D., Nagelli, E., Du, F., Dai, L. (2010). Metal-free carbon nanomaterials become more active than metal catalysts and last longer. *Journal of Physical Chemistry Letters*, 1(14), 2165–2173. DOI 10.1021/jz100533t.
52. Bag, S., Mondal, B., Das, A. K., Raj, C. R. (2015). Nitrogen and sulfur dual-doped reduced graphene oxide: synergistic effect of dopants towards oxygen reduction reaction. *Electrochimica Acta*, 163, 16–23. DOI 10.1016/j.electacta.2015.02.130.
53. Wang, Y. C., Wang, D. Y., Jiang, Y. T., Chen, H. A., Chen, C. C. et al. (2013). FeS₂ nanocrystal ink as a catalytic electrode for dye-sensitized solar cells. *Angewandte Chemie International Edition*, 52(26), 6694–6698. DOI 10.1002/anie.201300401.
54. Hou, Y., Wang, D., Yang, X. H., Fang, W. Q., Zhang, B. et al. (2013). Rational screening low-cost counter electrodes for dye-sensitized solar cells. *Nature Communications*, 4(1), 1583. DOI 10.1038/ncomms2547.
55. Liu, C. J., Tai, S. Y., Chou, S. W., Yu, Y. C., Chang, K. D. et al. (2012). Facile synthesis of MoS₂/graphene nanocomposite with high catalytic activity toward triiodide reduction in dye-sensitized solar cells. *Journal of Materials Chemistry*, 22(39), 21057–21064. DOI 10.1039/c2jm33679k.
56. Li, C. T., Wu, F. L., Lee, B. H., Yeh, M. C. P., Lin, J. T. (2017). Organic photosensitizers incorporating rigid benzo [1, 2-b: 6, 5-b'] dithiophene segment for high-performance dye-sensitized solar cells. *ACS Applied Materials & Interfaces*, 9(50), 43739–43746. DOI 10.1021/acsami.7b15181.
57. Zhang, Y., Hao, J., Li, J., Hao, C. (2016). Theoretical study of triiodide reduction reaction on nitrogen-doped graphene for dye-sensitized solar cells. *Theoretical Chemistry Accounts*, 135(1), 23. DOI 10.1007/s00214-015-1790-8.
58. Liu, Q., Li, Z. S., Chen, S. L. (2016). Metal-embedded graphene as potential counter electrode for dye-sensitized solar cell. *Industrial & Engineering Chemistry Research*, 55(2), 455–462. DOI 10.1021/acs.iecr.5b03464.